

# Electroosmotic Flow Phenomena in Packed Capillaries: From the Interstitial Velocities to Intraparticle and Boundary Layer Mass Transfer

U. Tallarek,<sup>\*,†,‡</sup> E. Rapp,<sup>‡</sup> A. Seidel-Morgenstern,<sup>‡</sup> and H. Van As<sup>†</sup>

Laboratory of Biophysics and Wageningen NMR Centre, Wageningen University, Dreijenlaan 3, 6703 HA Wageningen, The Netherlands, and Institut für Verfahrenstechnik, Otto-von-Guericke Universität Magdeburg, Universitätsplatz 2, 39106 Magdeburg, Germany

Received: March 1, 2002

Pulsed field gradient nuclear magnetic resonance studies of electrokinetic flow through a 250  $\mu\text{m}$  i.d. cylindrical fused-silica capillary packed with spherical porous particles ( $d_p = 41 \mu\text{m}$ ) have revealed the following phenomena and parameters: (i) An electrokinetic wall effect exists due to a mismatch of zeta-potentials associated with the capillary inner wall and the particles surface. It results in a transcolumn velocity profile which depends on the column-to-particle diameter ratio and causes additional longitudinal dispersion. (ii) Compared to the pressure-driven flow through the porous medium, the intraparticle mass transfer rate constant is significantly increased under the influence of a potential gradient. This increase also depends on the buffer concentration via electric double layer overlap. (iii) Fluid molecules in the porous particles remain diffusion-limited in the presence of a pressure gradient. By contrast, intraparticle Peclet numbers above unity have been measured for electroosmotic flow and were found to increase with the applied potential difference. (iv) Interparticle resistance to mass transfer appears to vanish on the pore scale when electric double layers are small compared to the relevant pore dimension.

## Introduction

Hydrodynamic dispersion in porous media arises from the nonuniformity of the flow pattern and depends on the morphology (geometry and topology) of the pore space including stagnant and low-permeability zones, the actual flow conditions (Reynolds and Peclet numbers), interactions with the surface (adsorption and/or reaction), and the type of liquid flow. In this last respect it has been recognized that a strong, stable electroosmotic flow (EOF) can offer many advantages over pressure driven flow in bulk transport of liquid through fixed beds of fine particles and other granular or fibrous media.<sup>1,2</sup> The dynamics of EOF through a single straight cylindrical capillary includes the following features:

(a) For thin electric double layers, i.e., Debye lengths  $\lambda_D$  much smaller than the capillary radius  $r_c$ , the fluid moves as in plug flow, i.e., the velocity apparently slips at the wall.<sup>3,4</sup> Thus, the correlation length of velocity extremes in the flow field can be very small. Axial dispersion and boundary layer mass transfer may become negligible compared to Poiseuille flow, which has been shown theoretically<sup>5,6</sup> and experimentally.<sup>7,8</sup>

(b) The ratio of electroosmotic to hydraulic flow rates at a fixed potential and pressure gradient is proportional to  $r_c^{-2}$  which has an important implication for electroosmotic perfusive flow through porous media: Mass transfer usually covers a hierarchy of lengthscales and the EOF becomes increasingly effective in liquid transport through finer channels as their size is reduced (if  $\lambda_D \ll r_c$  still holds). Thus, the spatiotemporal dimension of diffusion-limited mass transfer can be drastically reduced.

Basic applications of these EOF characteristics are mainly found in fluid and solute transport through porous media of low hydraulic conductivity, in cases where still a high volumetric throughput (not only by preferential channelling through the largest pores) and/or little flow field dispersion is mandatory. Those media often have a high electroosmotic conductivity and the EOF is insensitive to pore size and its distribution over a wide range of conditions.

Potential areas include miniaturized separation techniques such as capillary electrochromatography (CEC)<sup>9–13</sup> or environmental processes that use the electrokinetics for in situ remediation of fine-grained soils.<sup>14–17</sup> In CEC, 75–150  $\mu\text{m}$  i.d. fused-silica capillaries are packed with 3–5  $\mu\text{m}$  spherical, porous adsorbent particles and electric fields up to 10<sup>5</sup> V/m are applied to drive the liquid and solute (most often charged molecules) through the bed. This journey consists of a complex interplay between electrokinetic driving forces (electroosmosis and electrophoresis) and specific interactions with the surface (adsorption and/or reaction). The mobile phase usually is a 0.5–10 mM buffer solution which gives  $\lambda_D$  on the order of 1–10 nm.<sup>18</sup>

Although capillaries<sup>19,20</sup> and unit cell models<sup>21–23</sup> have been successful in describing the behavior of homogeneous, diluted and spatially periodic systems, modelling the electrokinetics in concentrated, disordered, and fractured media appears to be more complex.<sup>24–26</sup> Further, in a fixed bed of spherical porous particles, for example, which represents a porous medium with rather discrete bidisperse pore structure due to the high correlation of interconnectivity between the inter- and comparatively small intraparticle pores, fluid transport can involve conditions under which  $\lambda_D$  is of the same order as the intraparticle pore size, but still much smaller than interparticle channels. Theories and experimental approaches thus need to resolve the subdomain and even pore-level EOF in hierarchically

\* To whom correspondence should be addressed. Address: Otto-von-Guericke Universität Magdeburg. Phone: +49 (0)391-67-18644. Fax: +49 (0)391-67-12028. E-mail: ulrich.tallarek@vst.uni-magdeburg.de.

<sup>†</sup> Laboratory of Biophysics and Wageningen NMR Centre.

<sup>‡</sup> Institut für Verfahrenstechnik.

structured media to address the microscopic and mesoscopic details of the velocity field underlying flow and dispersion on a macroscopic scale.

Our studies were motivated by the fact that little is known about pore-level (microscopic) flow profiles, the column cross-sectional (macroscopic) velocity heterogeneity, as well as intraparticle and boundary layer mass transfer in EOF through randomly packed beds with a far more complex fluid dynamics than in a single and straight cylindrical channel. For example, in a pore network individual segments differ with respect to their orientation  $\theta$  toward the electric field vector  $\mathbf{E}$ , even if they are otherwise identical. This causes driving-force discontinuities from pore to pore ( $\mathbf{E}_{\text{pore}} = \mathbf{E} \cdot \cos \theta$ ), and because the liquid phase is continuous and incompressible, it influences the actual flow profile and average velocity on a pore level. Thus, the local fluid momentum is balanced by an increase or decrease in pore pressure which may also develop as a consequence of a nonuniform local electric field intensity and surface defects, or if there exists a variation in hydraulic resistance within the medium.<sup>27–29</sup> On a macroscopic level a flow nonuniformity can be due to the fact that the  $\zeta$ -potential associated with the capillary inner wall ( $\zeta_w$ ) is, in general, different from that of the particles surface ( $\zeta_p$ ) and so should be their EOF.<sup>30,31</sup> This electrokinetic wall effect further depends on the column-to-particle diameter ratio.

One particular question is related to the actual magnitude of intraparticle EOF velocities in CEC with respect to their interparticle average. Both experimental<sup>32–39</sup> and theoretical<sup>31,40,41</sup> studies have recently demonstrated that a substantial gain in performance over pressure driven flow lies in the electroosmotic perfusion mechanism, i.e., in the generation of a significant EOF through the finer intraparticle pore network which, on the other hand, has a much lower hydraulic conductivity compared to the coarser interparticle pore network. Intraparticle EOF velocities have already been calculated by the use of network modeling, but could not be deduced from experimental studies so far, although the existence of a perfusive transport was clearly shown. This phenomenon has also consequences for the electrokinetics of colloidal suspensions consisting of aggregates which themselves contain a large number of discrete particles. In contrast to the assumptions in hard sphere models, these aggregates are actually permeable and conducting.<sup>42</sup>

The purpose of this paper is to reveal experimentally these characteristics of the EOF in a fixed bed of permeable particles. We have used pulsed field gradient nuclear magnetic resonance (PFG-NMR)<sup>43</sup> to study over discrete temporal and spatial domains the dynamics of single-phase EOF through a packed capillary. Our goal was the measurement of inter- and intraparticle velocities of the perfusive flow field, as well as intraparticle and boundary layer mass transfer.

## Materials and Methods

A 250  $\mu\text{m}$  i.d. (365  $\mu\text{m}$  o.d.) cylindrical fused-silica capillary (Polymicro Technologies, Phoenix, AZ) was packed with spherical shaped porous, hydrophilic particles (POROS 50-OH2 from PerSeptive Biosystems, Framingham, MA). The nearly Gaussian size distribution has been measured on a Coulter LS 130 (Beckman Coulter, Fullerton, CA) and is shown in Figure 1. The polystyrene–divinylbenzene matrix is coated with a graft copolymer, itself based on a copolymerization of epichlorohydrin and glycidol, to render the surface hydrophilic.<sup>44,45</sup> The intraparticle pore network consists of a set of gigapores (400–600 nm,  $d_{\text{pore}}/d_p > 10^{-2}$ ) which transect the particle with

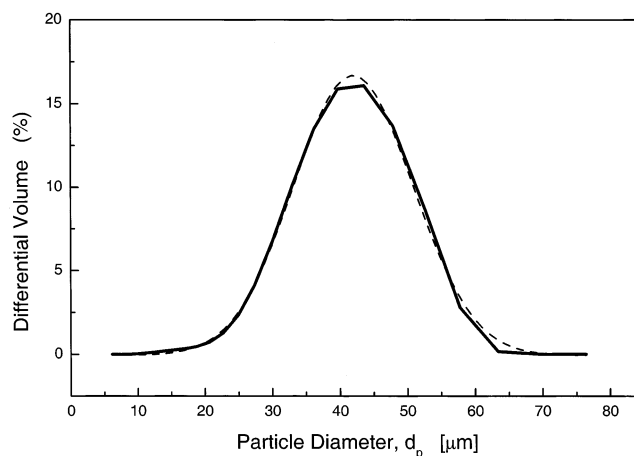


**Figure 1.** Size distribution of the spherical particles. Experimental data (solid line) represent an average of three independent measurements. Dashed line: Best Gaussian fit. The mean diameter is 41  $\mu\text{m}$ .

relatively little branching,<sup>46</sup> and smaller (50–100 nm) interconnecting macropores to enhance the surface area of the support for its use in chromatography.<sup>47</sup> Particles were packed as aqueous slurry for ca. 30 min at 100 bar in an ultrasonic bath. This procedure gave a dense packing without crushed particles (as validated by microscopic inspection). The whole capillary setup consisting of a packed and a connecting open segment was fritless, i.e., we used fused-silica capillaries with a conus in which the particles were held by a keystone effect during packing, without blocking the orifice.<sup>48</sup> Afterward, the tapered end of a 150  $\mu\text{m}$  i.d. open segment was fitted to the column outlet. This configuration (Figure 2) was absolutely stable over the 450 h of operation.

As the mobile phase in pressure driven flow and EOF we used thoroughly degassed sodium tetraborate buffer solutions of varying concentration without adding further electrolyte (pH 9.13, 25 °C). The Debye length is calculated according to

$$\lambda_D = \left( \frac{\epsilon_0 \epsilon_r R T}{F^2 \sum_i z_i^2 c_{i,\infty}} \right)^{1/2} \quad (1)$$

where  $\epsilon_0$  and  $\epsilon_r$  denote the permittivity of vacuum and the relative permittivity of the electrolyte solution, respectively.  $R$  is the gas constant,  $T$  the absolute temperature, and  $F$  Faraday's constant;  $z_i$  is the valency of ionic species  $i$  and  $c_{i,\infty}$  its concentration in electroneutral solution. At low concentrations sodium tetraborate is completely dissociated into equal amounts of boric acid and monoborate ion,<sup>49</sup> with an acid/base equilibrium between the two species.<sup>50</sup>



with



PFG-NMR measurements were performed on a spectrometer consisting of a 0.7 T ( $^1\text{H}$  30.7 MHz) electromagnet (Bruker, Karlsruhe, Germany) and an actively shielded magnetic field gradient system from Doty Scientific (Oak Harbor, SC), interfaced with a S. M. I. S. console. The packed capillary was fixed in a home-built radio frequency (r.f.) insert based on the solenoid.<sup>8</sup> In contrast to a superconducting magnet where the access down its symmetry axis requires saddle or birdcage r.f.

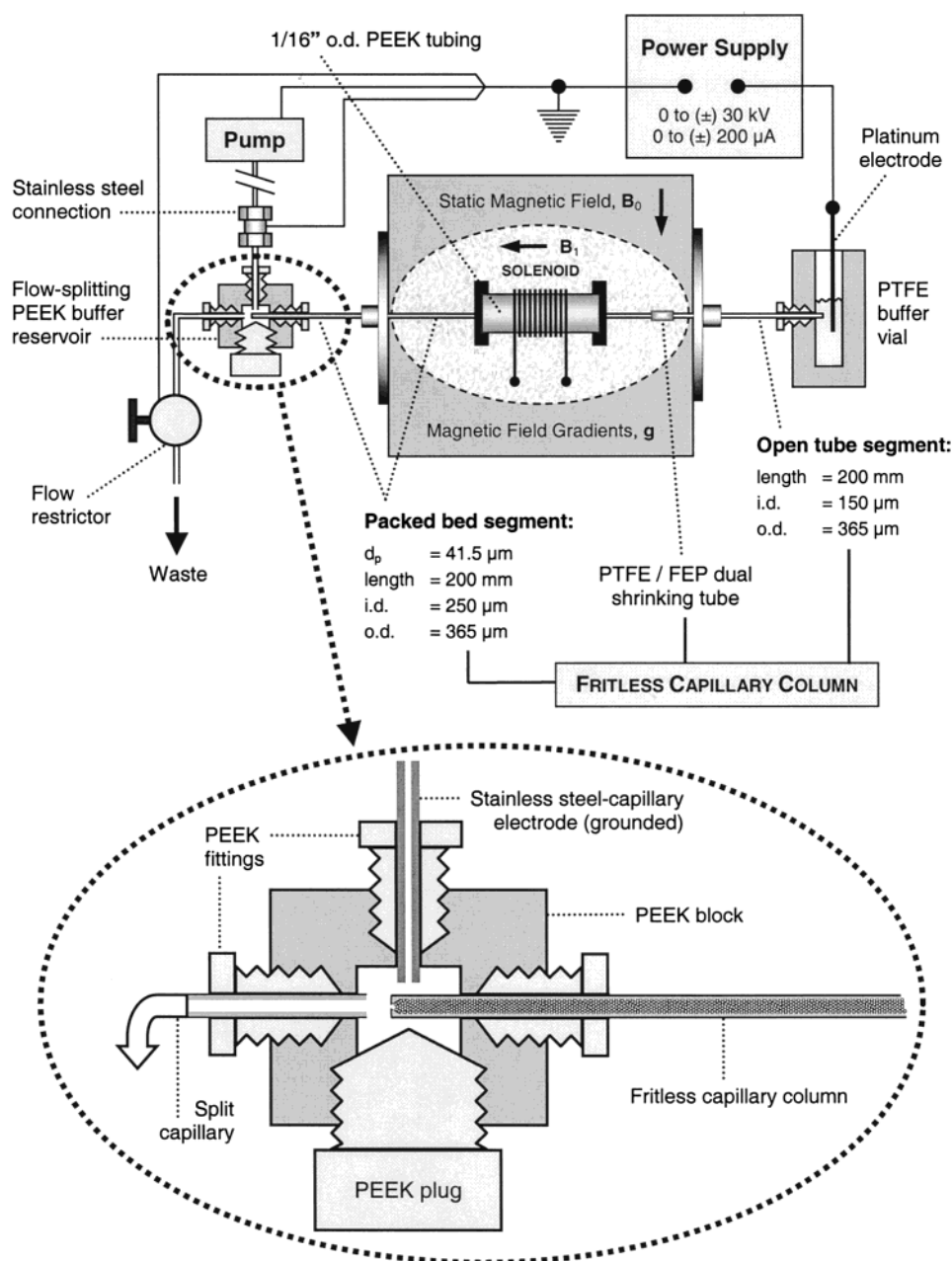


**Figure 2.** Experimental setup implemented for NMR measurements of fluid motion in electroosmotic and pressure driven flow through packed capillaries. The radio frequency ( $B_1$ ) field is provided by a ca. 11 mm long solenoid which is directly wound on a 35 mm long, 1.57 mm o.d. (381  $\mu\text{m}$  i.d.) PEEK tubing sleeve, itself accommodating the 360  $\mu\text{m}$  o.d. capillary. In pure electrokinetic flow, the split capillary is removed and the pump (at low volumetric flow rate) continuously refreshes buffer solution in the PEEK block, without inducing a measurable pressure gradient over the packed bed segment.

coil geometries<sup>43</sup> the electromagnet allows to use the more sensitive solenoid in a convenient axial orientation in the air gap of the magnet, facilitating the implementation and exchange of individual capillaries. For measurements involving a steady EOF through the bed the electrodes of a modular capillary electrophoresis instrument operating up to 30 kV and 200  $\mu\text{A}$  (Grom, Herrenberg-Kayh, Germany) were connected to the column by a home-built PEEK block (also acting as a flow splitter) on one side and a buffer reservoir through the open capillary segment on the other (Figure 2). Thus, a conventional HPLC pump could be used in pressure-driven flow.

For our studies we implemented the stimulated echo version of the PFG-NMR methodology.<sup>43</sup> With this combined radio frequency and gradient pulse scheme, the motion of fluid molecules is encoded by a pair of identical magnetic field

gradients of amplitude and direction  $\mathbf{g}$ , pulsed for a short time  $\delta$ , and separated by the experimental observation time  $\Delta$ . In the narrow gradient pulse limit,<sup>51</sup> i.e., for  $\delta \ll \Delta$ , the following relationship exists between the nuclear spin phase and position

$$\phi_i(\Delta) = \gamma \delta \mathbf{g} \cdot [\mathbf{r}_i(\Delta) - \mathbf{r}_i(0)] = \gamma \delta \mathbf{g} \cdot \mathbf{R}_i(\Delta) \quad (2)$$

where  $\gamma$  is the magnetogyric ratio of the nucleus considered ( $^1\text{H}$ ) and  $\mathbf{R}$  is the net displacement of spin  $i$  over time  $\Delta$  along the direction of  $\mathbf{g}$ . The total, normalized signal amplitude at the echo center is obtained by a summation over all individual spins in the measurement volume which (in propagator language) translates to

$$E(\mathbf{q}, \Delta) = \int P_{\text{av}}(\mathbf{R}, \Delta) \exp(i2\pi \mathbf{q} \cdot \mathbf{R}) d\mathbf{R} \quad (3)$$



with  $\mathbf{q} = (2\pi)^{-1} \gamma \delta \mathbf{g}$ ,  $P_{\text{av}}(\mathbf{R}, \Delta)$ , the average propagator, gives the probability that *any* molecule travels a net displacement  $\mathbf{R}$  over time  $\Delta$ .<sup>52</sup> It is related to the initial nuclear spin density and an equivalent to the Green function<sup>53</sup> by

$$P_{\text{av}}(\mathbf{R}, \Delta) = \int \rho(\mathbf{r}_0) P(\mathbf{r}, \Delta / \mathbf{r}_0) d\mathbf{r}_0 \quad (4)$$

$P(\mathbf{r}, \Delta / \mathbf{r}_0)$  is the conditional probability for finding a molecule at  $\mathbf{r}$  after time  $\Delta$  given that it was at  $\mathbf{r}_0$ .  $P_{\text{av}}(\mathbf{R}, \Delta)$  is reconstructed directly by Fourier transformation of  $E(\mathbf{q}, \Delta)$  with respect to  $\mathbf{q}$ . When the displacement distribution is a single Gaussian (and the exchange between velocity extremes in the flow field is complete) we obtain<sup>54,55</sup>

$$E(\mathbf{q}, \Delta) = \exp(i2\pi \mathbf{q} \cdot \mathbf{u}_{\text{av}} \Delta - 4\pi^2 q^2 D_{\text{a,t}} \Delta_{\text{eff}}) \quad (5)$$

where  $\mathbf{u}_{\text{av}}$  is the average mobile phase velocity through the bed.  $D_{\text{a}} (\mathbf{q} \parallel \mathbf{u}_{\text{av}})$  and  $D_{\text{t}} (\mathbf{q} \perp \mathbf{u}_{\text{av}})$  are the long-time, asymptotic axial and transverse dispersion coefficients which (for macroscopically isotropic porous media) satisfy the following form of the convection-diffusion equation describing dispersion of a passive tracer of macroscopic mean concentration  $\langle c \rangle$  in single-phase incompressible flow along the  $\mathbf{z}$ -direction<sup>56</sup>

$$\frac{\partial \langle c \rangle}{\partial t} + \mathbf{u}_{\text{av}} \cdot \nabla \langle c \rangle = D_{\text{a}} \frac{\partial^2 \langle c \rangle}{\partial z^2} + D_{\text{t}} \nabla_{\text{t}}^2 \langle c \rangle \quad (6)$$

When a complete exchange of fluid molecules between the intraparticle and interparticle pore space has not been achieved over time  $\Delta$ , both  $E(\mathbf{q}, \Delta)$  and  $P_{\text{av}}(\mathbf{R}, \Delta)$  reveal discrete bimodal behavior. It is most pronounced at flow rates high enough that convection dominates interparticle dispersion, while (typical for pressure-driven flow) the intraparticle fluid remains purely diffusive or at least diffusion-limited<sup>57,58</sup>

$$E(\mathbf{q}, \Delta) = \sum_{n=1}^2 A_n(\Delta) \exp(i2\pi \mathbf{q} \cdot \mathbf{u}_n \Delta - 4\pi^2 q^2 D_n \Delta_{\text{eff}}) \quad (7)$$

The fractions  $A_n(\Delta)$  represent unexchanged intraparticle fluid molecules ( $A_{\text{intra}}$ ) and those having experienced interparticle flow ( $A_{\text{inter}}$ ). If the coefficients  $D_n$  characterizing dispersive motion are sufficiently different (usually  $D_{\text{intra}} \ll D_{\text{inter}}$  because  $u_{\text{intra}}/u_{\text{inter}} \rightarrow 0$ ),  $A_{\text{intra}}$  and the intraparticle mass transfer kinetics can be determined. By using eq 7 for that purpose we have corrected for the nuclear spin-spin and spin-lattice relaxation times, as described earlier.<sup>58</sup> Our  $^1\text{H}$  PFG-NMR measurements were performed with 40  $\mathbf{q}$ -steps equally spaced between  $\pm \mathbf{q}_{\text{max}}$  taking up to 64 averages at each value of  $\mathbf{q}$  ( $\delta = 2.5$  ms and  $\Delta_{\text{eff}} = \Delta - \delta/3$ ).

## Results and Discussion

As a goal of this work is to contrast between electroosmotic and pressure driven flow concerning velocity extremes of the flow field in a bed of spherical, permeable particles, Figure 3 begins to illustrate the dynamics of intraparticle diffusion and interparticle convection for laminar flow when  $\Delta < r_p^2/2D_{\text{intra}}$  ( $r_p$  is the particle radius). In liquid chromatography the intraparticle pores are typically a factor  $10^2$ – $10^3$  smaller than the interparticle channels.<sup>59</sup> By considering a particle itself as an aggregate of microparticles, a permeability estimate obtained with the Carman-Kozeny equation<sup>60</sup> suggests that intraparticle convection is not an important transport mechanism compared to molecular diffusion unless the pressure drop becomes exceedingly high and the solute diffusivity low or, of course,

as  $d_{\text{pore}}/d_p$  increases significantly. Thus, intraparticle mass transfer is diffusive over a relatively wide range of conditions, and because the fluid molecules are small compared to the particles pore dimension (and usually nonsorbed on their surface),  $D_{\text{intra}}$  is related to the molecular diffusivity just by the tortuosity factor  $\tau_{\text{intra}}$  (Figure 3). On the particle-scale (there is no need to resolve beyond this level in the present work)  $\tau_{\text{intra}}$  is a parameter accounting for the *effective* pore network topology and lumps together distributions of pore size, pore shape, surface defects, and pore interconnectivity. Diffusive intraparticle liquid holdup in pressure-driven flow may constitute the most significant mechanism for transient and asymptotic axial dispersion in macroscopically homogeneous beds at flow rates where convective times ( $\tau_C = u_{\text{av}}\Delta/d_p$ ) well exceed the dimensionless time for diffusion ( $\tau_D = D_{\text{intra}}\Delta/d_p^2$ ).<sup>61</sup>

To leave a particle completely and join the interparticle streamlines a molecule that starts at the spheres center diffuses through the intraparticle pore network and a diffusive boundary layer at the particles external surface (Figure 3). This leads to a characteristic exchange time  $\Delta_e$  based on  $r_p$ ,  $D_{\text{intra}}$ , and, strictly, also on the thickness of the boundary layer ( $\delta_f$ ), which is an inverse function of the flow rate (although in most cases  $\delta_f \ll r_p$ ). Boundary layer mass transfer manifests itself in the measurements by a distance over which diffusion normal to the solid-liquid interface remains comparable to convective transport parallel to it (Figure 3), while the velocity is zero *at* the surface due to the no-slip condition. It should be noted that  $D_{\text{intra}}$  obtained by PFG-NMR is based on a direct measurement of intraparticle displacements and, consequently, does not account for the spheres porosity ( $\epsilon_{\text{intra}}$ ).  $D_{\text{intra}}$  can be related to the often used effective diffusivity (as observed from “outer”, i.e., the interparticle pore space) by  $D_{\text{eff}} = \epsilon_{\text{intra}} D_{\text{intra}}$ .

Figure 4a,b show displacement probability distributions of the fluid molecules in laminar flow through the packed capillary. While at 20 ms a substantial fluid fraction still remains unexchanged inside the particles, it becomes less than 5% after 150 ms and is only visible as the shoulder around zero displacement (Figure 4b). By recording the amount of intraparticle-only fluid as a function of  $\Delta$ , a mass transfer rate constant  $B_{\text{intra}} = \pi^2 D_{\text{intra}}/r_p^2$  can be determined from the well-known model describing the purely diffusive emptying of spheres under the assumption of constant boundary conditions<sup>62</sup>

$$\frac{A_{\text{intra}}(\Delta)}{A_{\text{intra}}(0)} = \frac{6}{\pi^2} \sum_{n=1}^{\infty} \frac{1}{n^2} \exp(-n^2 B_{\text{intra}} \Delta) \quad (8)$$

The data shown in Figure 4c are well described by eq 8 and give  $D_{\text{intra}} = 1.36 \times 10^{-5} \text{ cm}^2 \text{ s}^{-1}$ . Thus,  $\tau_{\text{intra}} = D_{\text{m}}/D_{\text{intra}} = 1.65$ , in good agreement with tortuosity factors reported recently for similar supports.<sup>58,63,64</sup> It should be recalled that the PFG-NMR method, in contrast to most conventional tracer techniques, detects the complete displacement spectrum of instantaneously *physically* labeled molecules ( $^1\text{H}_2\text{O}$ ) residing in an equilibrium with respect to their local concentration, i.e., *chemically* the mobile phase is (and continues to be) perfectly mixed. As the pore size distribution of the particles is actually bimodal<sup>47,65</sup> the intraparticle mass transfer kinetics could reveal a corresponding two-component behavior, depending on the characteristic time constants for diffusion in either set of pores.<sup>66</sup> However, because already the shortest observation time in our work ( $\Delta = 15$  ms) gives a root-mean-squared translational displacement of the order of  $8 \mu\text{m}$ , which is larger than the spatial domain of both the macro- and gigaporous network,<sup>47,65</sup>  $D_{\text{intra}}$  in eq 8 is expected to represent effective diffusion in a

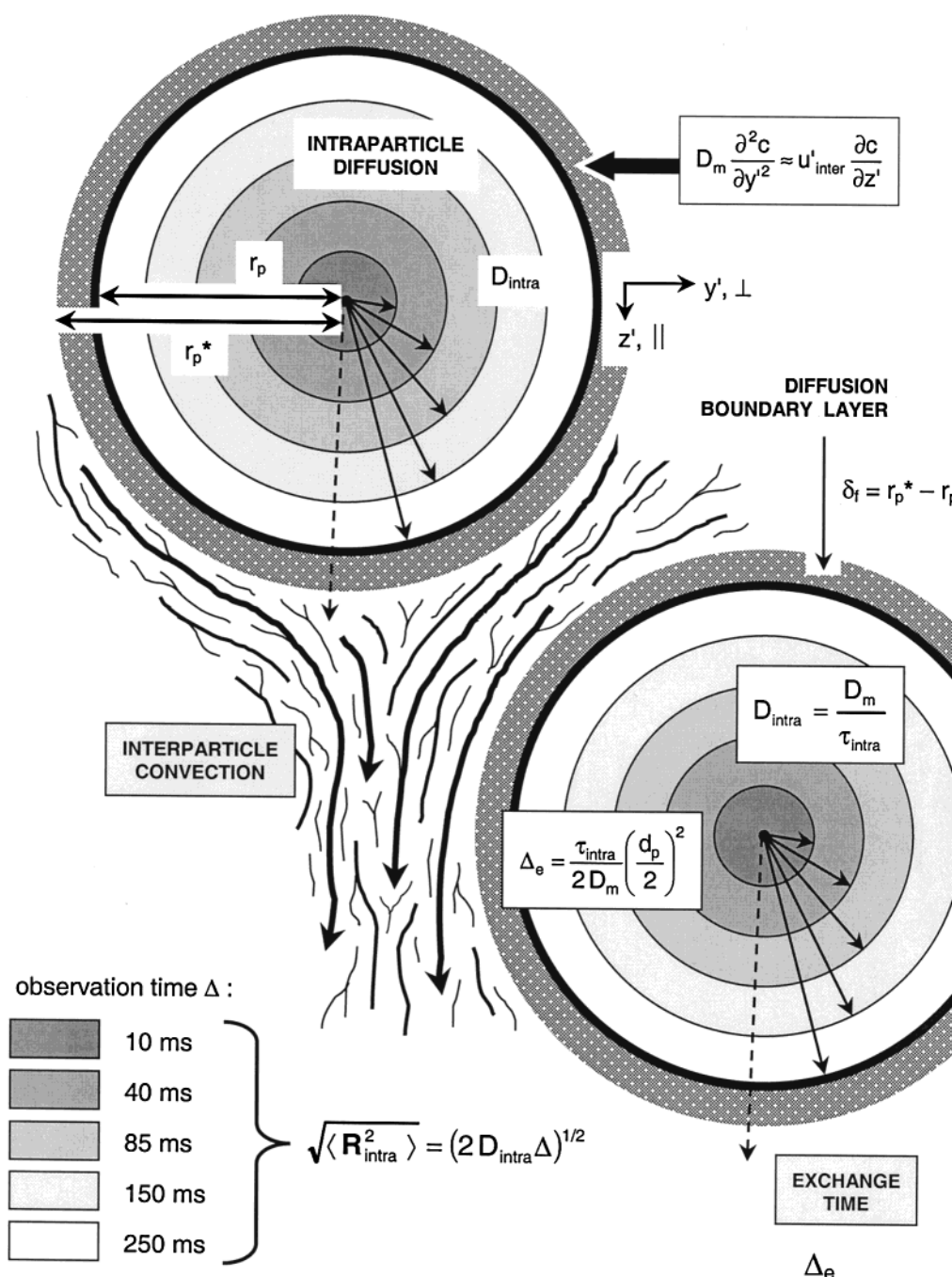


**Figure 3.** Dynamics of fluid in viscous flow through a fixed bed of porous spherical particles, including interparticle convection, intraparticle diffusion and boundary layer mass transfer associated with the no-slip condition at the solid–liquid interface ( $u'_{inter}$  is the local velocity component parallel to the particles external surface). Model parameters:  $d_p = 50 \mu\text{m}$ ,  $D_m = 2.25 \times 10^{-5} \text{ cm}^2 \text{ s}^{-1}$ ,  $\tau_{intra} = 1.8$ .

hierarchically structured intraparticle network of giga- and macropores. This is supported by earlier studies which have demonstrated that  $D_{intra}$  has indeed reached the tortuosity asymptote at this observation time,<sup>58</sup> in agreement with the data in Figure 4c revealing a constant value for  $D_{intra}$ .

Concerning diffusion-limited mass transfer in pressure driven flow it should be noted that if a small intraparticle velocity component indeed exists (even strong enough to dominate the transport of slowly diffusing tracers in the flow field) our measurements are relatively insensitive for its contribution to the overall kinetics as the diffusivity of flow field molecules is several orders of magnitude higher than those of large tracers such as proteins.<sup>67</sup> Thus, our intraparticle mass transfer data are necessarily obtained in the tortuosity-limited regime ( $D_{intra}$

$< D_m$ ), where transport is dominated by diffusion, but they cannot exclude the existence of a comparatively small convective driving force inside the particles.

After having started with the discrete bimodal propagator distribution in pressure driven flow (Figure 4a) which results from the large differences in hydraulic conductivity of the intra- and interparticle pore networks we turn to electrokinetically driven flow through the packing.  $P_{av}(\mathbf{R}, \Delta)$  in Figure 5 reveals a skewed Gaussian with significant fronting and the intraparticle fluid is not resolved as a separate peak. One reason for that observation is that the maximum driving force (electric potential gradient) now is relatively limited (30 kV) compared to the pressure gradient ( $\leq 80 \text{ bar}$ ) in the former case. Thus, even when the electroosmotic conductivities of the intra- and interparticle

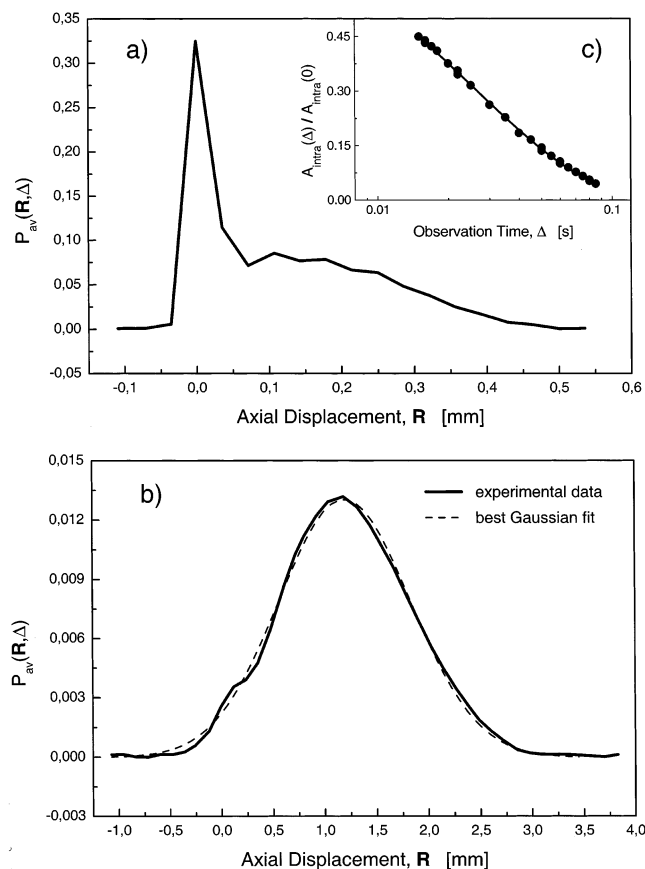


**Figure 4.** Pressure driven flow through the packed capillary, displacement distributions for (a)  $\Delta = 20$  ms and (b)  $\Delta = 150$  ms. (c) Intraparticle mass transfer kinetics (from 15 to 85 ms, upper limit given by the signal-to-noise ratio), solid line: Best fit of the data to eq 8. Pressure gradient:  $\Delta P = 45$  bar,  $Pe = u_{av}d_p/D_m = 145$ ,  $Re = u_{av}d_p\rho/\eta = 0.36$  (kinematic viscosity:  $\eta/\rho = 8.9 \times 10^{-3}$  cm<sup>2</sup> s<sup>-1</sup> at 25 °C),  $r_p = 20.5$   $\mu$ m,  $D_m = 2.25 \times 10^{-5}$  cm<sup>2</sup> s<sup>-1</sup>, and  $B_{intra} = \pi^2 D_{intra}/r_p^2 = 31.7$  s<sup>-1</sup>.

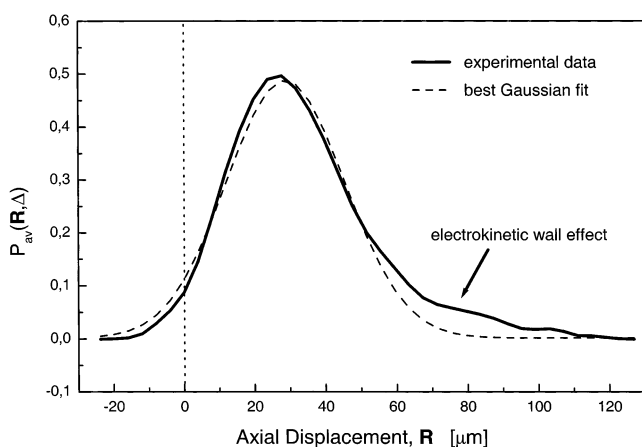


**Figure 5.** Electrokinetically driven flow through the packed capillary. Mobile phase:  $2 \times 10^{-3}$  M sodium tetraborate solution ( $E = 47.4$  kV m<sup>-1</sup>,  $I = 53$   $\mu$ A, and  $\Delta = 40$  ms).

pore networks differ significantly, a corresponding displacement discrimination could probably not be achieved. However, because of the small fluid fraction that is actually left around zero displacement and the substantial character in  $P_{av}(R, \Delta)$  of a very narrow Gaussian (Figure 5), this result rather suggests that electroosmotic conductivities of the respective pore networks are indeed similar and for that reason prevent a discrete visualization of the intraparticle fluid. Concluding already from

Figure 5, it is not possible to resolve intraparticle fluid and study the associated mass transfer in *pure* electrokinetic flow. A more promising strategy for measuring the influence of a potential gradient on intraparticle mass transfer is to apply a sufficient pressure gradient, as in Figure 4a, then *add* a potential gradient and follow its effect on fluid exchange (cf. Figure 4c), using the pure hydraulic flow data as diffusive reference.

Before doing that in detail we try to understand the pronounced fronting of  $P_{av}(R, \Delta)$  seen in Figure 5. EOF in the packed column originates in the Debye layer close to solid–liquid interfaces (where the buffer solution is locally charged) through a body force on the liquid caused by the externally applied electric field. Surfaces in contact with the liquid are those of the particles and capillary inner wall. These, however, not only differ in their chemical nature, but also concerning physical properties including the electrokinetics represented by the  $\zeta$ -potential. Thus, depending on  $\zeta_{ex} = (\zeta_w - \zeta_p)$  and the actual column-to-particle diameter ratio,  $\psi = d/d_p$ , the resulting macroscopic flow heterogeneity<sup>30,31</sup> will engender additional dispersion. Due to the low aspect ratio ( $\psi \approx 6$ ) this effect is aggravated in the present case. Although the particles surface and capillary inner wall both carry a negative charge density, the (open) fused-silica capillaries are known to give EOF velocities which are significantly higher than those of many packing materials used in CEC, even after having corrected for the packed beds tortuosity factor.<sup>68–70</sup> The fronting behavior in Figure 5 is an electrokinetic phenomenon and cannot be explained by the open segment via a flow-equalizing intersegmental pressure that develops due to the conservation of volumetric flow rate for an incompressible liquid in the whole capillary setup as the hydraulic permeability of the packed segment is far too low compared to that of the open channel.<sup>71</sup> For our capillary configuration (Figure 2) we calculate a pressure difference between the open and packed segments of well below 1 bar,<sup>71</sup> insufficient to drive any measurable amount of liquid through the bed. The influence of the capillary wall on a radial distribution of EOF velocities may be estimated by<sup>30,31</sup>

$$\frac{u_{inter}(r)}{u_p} = 1 + \left( \frac{\zeta_w}{\zeta_p} - 1 \right) \frac{I_0(\beta r/d_p)}{I_0(\beta r_{eff}/d_p)} \quad \text{for} \quad 0 \leq r \leq r_c - 7\lambda_D \cong r_{eff} \quad (9)$$

$I_0$  is the zero-order modified Bessel function of the first kind,  $r_{eff}$  is an effective capillary radius (accounting for the no-slip condition at the inner wall of the column), and  $\beta$  characterizes the overall permeability of the bed.<sup>72</sup> Although the underlying model<sup>30,31</sup> may be refined by considering the actual radial porosity distribution close to the wall and its consequences for the *local* permeability in this critical region,<sup>73,74</sup> Figure 6 demonstrates the strong effect of  $\zeta_w/\zeta_p$  on transcolumn EOF profiles ( $\psi = 6$ ). The most striking result is that  $\zeta_w$  may even prevent attainment of  $u_p$  in the center of the bed.

Compared to these predictions Figure 7 illustrates the driving force dependence of the propagator shape and the consequences for axial dispersion observed in our measurements. As the electric field strength is increased (Figure 7a) the wall component becomes first visible through a decent shoulder (e.g.,  $E = 21.1$  kV m<sup>-1</sup>), but it still leaves the average propagator substantially Gaussian. Upon further increase, however,  $P_{av}(R, \Delta)$  deteriorates to a broad distribution (Figure 7b) and displacements of the fastest fluid molecules in the wall annulus (propagator front) are more than 3 times higher than those moving in the central core region of the bed (see arrows). The clean velocity field would probably reveal an even larger difference between



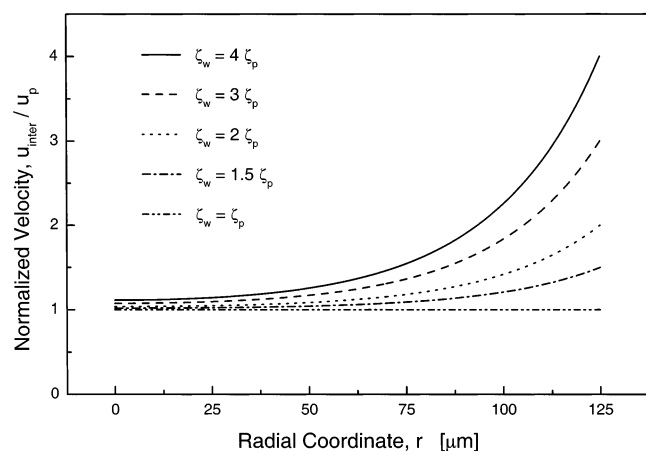


**Figure 6.** Column cross-sectional EOF profiles predicted by eq 9 with  $r_c = 125 \mu\text{m}$ ,  $d_c/d_p = 6$ ,  $\lambda_D = 3.9 \text{ nm}$ , and  $\beta = 1.65$  ( $u_p$  is the velocity associated with the particles surface only, according to  $\zeta_p$ ).

wall ( $\zeta_w$ ) and bed ( $\zeta_p$ ) components because molecular diffusion tends to blur the spectrum of instantaneous velocities. The spatial dimension of the “wall annulus” is the distance from the capillary surface over which the local fluid velocity is affected by  $\zeta_w$ . The resulting macroscopic flow heterogeneity needs a transcolumn equilibration of fluid molecules, i.e., exchange via lateral dispersion over the full capillary radius to approach a single, uniform Gaussian. Similar to  $P_{av}(\mathbf{R}, \Delta)$  in Figure 7b, the corresponding amplitude modulation of  $E(\mathbf{q}, \Delta)$  shown in Figure 7c reveals a bimodal behavior. Using eq 7 to calculate the apparent dispersion coefficient  $D_{ap,a}(\Delta)$  of either fluid-element ensemble it becomes evident that dispersion in the wall annulus is significantly higher than in the center of the column (Figure 7c). Thus, in the limit  $\Delta > r_c^2/2D_i$ , the wall effect has obscured an otherwise outstanding dispersion characteristics of the EOF in the packed bed region indicated by the narrow Gaussian core of  $P_{av}(\mathbf{R}, \Delta)$  (Figures 7a–c).

While the bimodal behavior in pressure driven flow reflects intraparticle stagnation (Figure 4a), it addresses a macroscopic flow heterogeneity with EOF (Figure 5). Although wall effects caused by a nonuniform radial porosity distribution are well-known in the former case,<sup>73,74</sup> the low intraparticle velocity here dominates the appearance of  $P_{av}(\mathbf{R}, \Delta)$  at relatively high Pe compared to the situation with EOF where the intraparticle mass transfer is obviously faster (for reasons that we still have to demonstrate) and the wall effect becomes more pronounced and/or discrete. Recently, electrokinetic wall effects and those encountered in hydraulic flow have been spatially resolved by dynamic NMR microscopy with  $40 \mu\text{m}$  in-plane resolution in a study of fluid flow through a  $250 \mu\text{m}$  i.d. capillary packed with  $50 \mu\text{m}$  cation exchange particles.<sup>75</sup> In both cases (but for different reasons) wall effects severely affected transient dispersion, causing a long-time disequilibrium in the axial displacement distribution which significantly exceeds the time scale of intraparticle mass transfer. In this context, the recent NMR imaging studies of Locke et al.<sup>76</sup> on spatial variations of the EOF velocity field in porous media (with a  $78 \times 78 \mu\text{m}^2$  resolution in  $100 \mu\text{m}$  thick slices) and of Sederman et al.<sup>77</sup> on the structural characterization of the interparticle void space in fixed beds should also be mentioned.

After having explained the fronting behavior of  $P_{av}(\mathbf{R}, \Delta)$  in EOF at low aspect ratio, we focus on the influence of a potential gradient on intraparticle fluid transport. Figure 8 compares the mass transfer kinetics obtained in pressure-driven flow with the effect of an *additional* potential gradient at increasing buffer concentration. It is evident that the electric field significantly

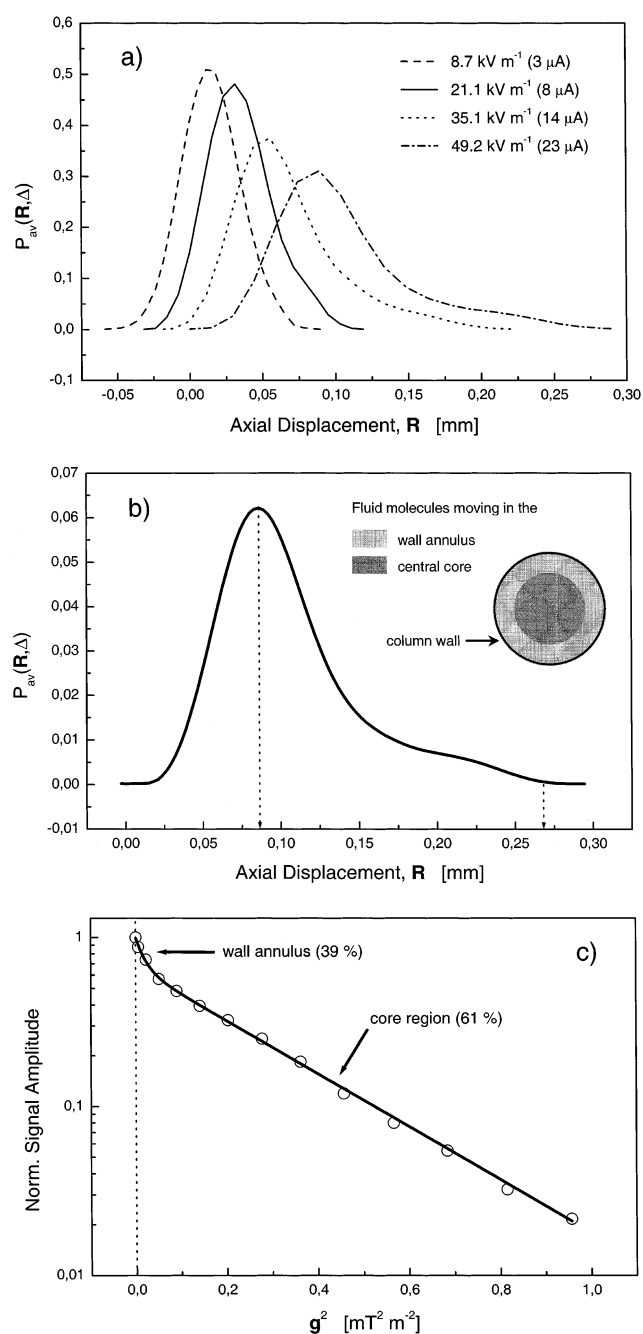


**Figure 7.** Electrokinetic wall effect. (a) Propagator distributions as a function of the electric field strength ( $\Delta = 120 \text{ ms}$ ,  $10^{-3} \text{ M}$  buffer), (b) last measurement ( $49.2 \text{ kV m}^{-1}$ ,  $23 \mu\text{A}$ ) with 10 times zero-filling in  $\mathbf{q}$ -space prior to Fourier transformation. (c) Best fit of the normalized echo attenuation function in  $E(\mathbf{q}, \Delta)$  to eq 7, revealing fluid molecules in the wall annulus ( $D_{ap,a} = 4.29 \times 10^{-4} \text{ cm}^2 \text{ s}^{-1}$ ) and the beds central core ( $D_{ap,a} = 3.5 \times 10^{-5} \text{ cm}^2 \text{ s}^{-1}$ ).

enhances the exchange of fluid molecules between intra- and interparticle pore networks (even compared to diffusion on the flow field level) and that, further, the intraparticle mass transfer rate constant (still obtained from eq 8) increases with the buffer concentration. This increase can be caused by one or a combination of the following factors: (i) double-layer overlap inside the particles is reduced thereby increasing volumetric EOF, (ii) an increased amount of borate ions adsorbs on the surface and increases  $\zeta_p$ , (iii) molecular diffusion is increased by thermal effects in the capillary which are aggravated by an increase of  $c_B$  (at constant  $E$ ). It is important to note that, while the first two phenomena point toward an intraparticle convection,

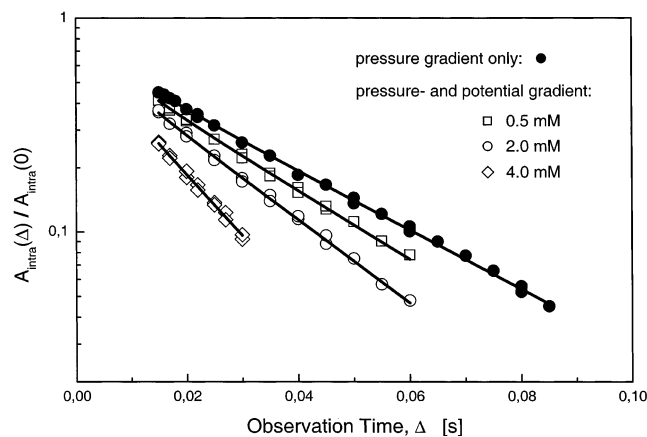


**Figure 8.** Intraparticle mass transfer kinetics. Influence of a pressure- and superimposed potential gradient ( $E = 47.4 \text{ kV m}^{-1}$ ) on fictitious emptying of the spherical particles. Column pressure drop,  $\Delta P = 45 \text{ bar}$  ( $Pe = 145$ ). Solid lines are best fits of the data to eq 8.

**TABLE 1: Intraparticle Mass Transfer Characteristics ( $E = \text{constant}$ )<sup>a</sup>**

$c_B [10^{-3} \text{ M}]$	0.5	1	2	2 <sup>b</sup>	3	4
$B_{\text{intra}}^{\text{ap}} [\text{s}^{-1}]$ , eq 8	36.9	40.3	45.2	44.3	55.9	64.6
$\lambda_D [\text{nm}]$ , eq 1	7.8	5.5	3.9	3.9	3.2	2.7

<sup>a</sup>  $E = 47.4 \text{ kV m}^{-1}$ ,  $Pe = 145$  ( $\Delta P = 45 \text{ bar}$ ), and  $Re = 0.36$  unless stated otherwise. <sup>b</sup>  $Pe = 50$  ( $\Delta P = 15 \text{ bar}$ ) and  $Re = 0.12$ .

the last aspect leaves mass transfer purely diffusive. Most relevant parameters of this measurement series are summarized in Table 1. In general, intraparticle mass transfer may be due to a combination of diffusion *and* convection. These mechanisms are characterized by different driving forces and the concentric circles seen in Figure 3 (representing purely diffusive transport in the radial direction with a constant  $D_{\text{intra}}$ ) lose their spherical symmetry, because convection in the sphere occurs along the axial direction.<sup>78–80</sup> For an approximate calculation of a now *apparent* mass transfer rate constant  $B_{\text{intra}}^{\text{ap}}$  based on the continued use of eq 8, our analysis neglects this geometrical aspect. It further does not realize convection as an independent transport mechanism, but relies on the simplifying concept of a convection-augmented diffusivity.<sup>81–83</sup> An exact, but more difficult to use analytical solution for the simultaneous transient diffusion and convection in spherical particles has been reported by Carta et al.<sup>67</sup> and was extended by Lu et al.<sup>79</sup> to include first-order reaction.

Double layer overlap inside the particles occurs mainly in the macropores ( $r_{\text{pore}} = 25\text{--}50 \text{ nm}$ ), to a lesser extent also in the gigapores ( $r_{\text{pore}} = 200\text{--}300 \text{ nm}$ ). The electric double layer is “thin” compared to the pore dimensions when  $r_{\text{pore}}/\lambda_D > 100$ . This ratio influences the pore-level profile in electrokinetic flow and also governs volumetric transport through a pore.<sup>3</sup> It ranges between 3.2 ( $c_B = 5 \times 10^{-4} \text{ M}$ ) and 18.5 ( $c_B = 4 \times 10^{-3} \text{ M}$ ) for the macropores and between 25.6 and 111 for the gigapores. Thus, while we expect substantial EOF in the gigaporous network, little affected by the electrolyte concentration over the range studied, volumetric EOF through the macroporous network should sensitively depend on  $r_{\text{pore}}/\lambda_D$  and increase significantly with  $c_B$  (cf. Table 1).<sup>84</sup> In the limit of a “totally perfusive regime” (which is not even reached in the present work) we have  $r_{\text{pore}}/\lambda_D > 100$  for *any* set of inter- and intraparticle pores, i.e., the complete (interconnected) pore space is permeated by EOF with maximum velocities and volumetric flow rates. This, in turn, addresses the importance of a favorable network topology including high interconnectivity and a small amount of dead-end pores.<sup>38,41</sup>

Concluding from these considerations a suppression of double layer overlap is definitely an issue in view of the observed increase of  $B_{\text{intra}}^{\text{ap}}$  with  $c_B$ . Also mentioned in Table 1 is  $B_{\text{intra}}^{\text{ap}}$  obtained from a set of measurements ( $c_B = 2 \times 10^{-3} \text{ M}$ ) which were conducted with a significantly reduced pressure gradient ( $\Delta P = 15 \text{ bar}$ ), but identical potential gradient ( $E = 47.4 \text{ kV m}^{-1}$ ). In general, the effective  $Pe$  depends on  $\Delta P$  and  $E$ . When comparing the data for  $Pe = 50$  and  $Pe = 145$  ( $\Delta P = 15$  and  $45 \text{ bar}$ ) it is clear that a change in column pressure drop hardly influences the intraparticle mass transfer kinetics. On the other hand, it is well-known that the “thickness” of the boundary layer in low- $Re$ , high- $Pe$  ( $Pe > 50$ ) pressure-driven flow through the bed (cf. Figure 3) is an inverse function of the flow rate<sup>85</sup> and, as such, can explain a dependence of stagnant mobile phase mass transfer on  $Pe$  in cases where intraparticle forced convection is too small to account for it.<sup>58,86</sup> Thus, our observation implies that boundary layer mass transfer is negligible in EOF because  $B_{\text{intra}}^{\text{ap}}$  is essentially unaffected when  $Pe$  is varied via the pressure gradient (at constant  $E$ ). By returning to the ideal and comparatively simple situation encountered in a straight single capillary, this result can be understood by the spatial dimension of the velocity boundary layer in either type of liquid flow.<sup>1</sup> While for EOF through micrometer channels,  $r_{\text{pore}}/\lambda_D > 100$  can be easily achieved experimentally and the maximum (plug-flow) pore velocity is already reached after a few nanometers from the surface<sup>31</sup> ( $\approx 7\lambda_D$ ) by lateral diffusion, the velocity (viscous) boundary layer in Poiseuille flow covers the whole radius of the capillary.<sup>7,8</sup> It also suggests that diffusive mass flux normal to the surface remains competitive to convective transport parallel to it over a considerably longer distance than in EOF. Concerning laminar flow through a packed bed stagnant fluid in the *interparticle* pore space may be visualized as a hydrodynamic layer around the particles with a thickness that in pressure driven flow can reach a few percent of the particle radius,<sup>58,86</sup> depending on  $Pe$ ,  $Re$ , and the actual density of the packing. By contrast, practically all fluid molecules beyond the electric double layer move with a significant velocity in electrokinetically driven flow (at high  $E$ ,  $\epsilon_r$ , and  $\zeta_p$ ) when compared to diffusion, including those in cusp regions between particles where much of the interparticle fluid side resistance to mass transfer is located in pressure driven flow.

Returning to intraparticle mass transfer, values for  $B_{\text{intra}}^{\text{ap}}$  (Table 1) even leave the tortuosity-limited regime (for  $c_B \geq 3 \times 10^{-3} \text{ M}$ ). It may be partly due to a reduced double layer overlap in the macropores, but because the temperature increase of the buffer solution is also most pronounced at high  $c_B$  we still need a measurement that distinguishes clearly between purely diffusive mass transfer (at any temperature) and intraparticle EOF. As the level of heat dissipation in the capillary is represented by the product of electric field strength and current, we kept  $EI$  constant in a new series of measurements at increasing buffer concentration. By adjusting  $E$  for every  $c_B$  such that  $EI$  holds the selected value ( $2.54 \text{ W m}^{-1}$ ), this not only ensures a constant thermal niveau in the capillary but also gives a systematic variation of  $E$ , the electrokinetic driving force, depending on  $c_B$ . The results shown in Figure 9a demonstrate that  $B_{\text{intra}}^{\text{ap}}$  increases significantly with  $E$ . Because thermal effects are now constant and do not explain this increase by the temperature dependence of  $D_m$ , only a convective transport mechanism can be responsible for the enhancement of intraparticle mass transfer (Table 2). When extrapolating these data to zero electric field strength the value for  $B_{\text{intra}}^{\text{ap}}$  (about  $33.5 \text{ s}^{-1}$ , see dotted line in Figure 9a) represents the case of pressure



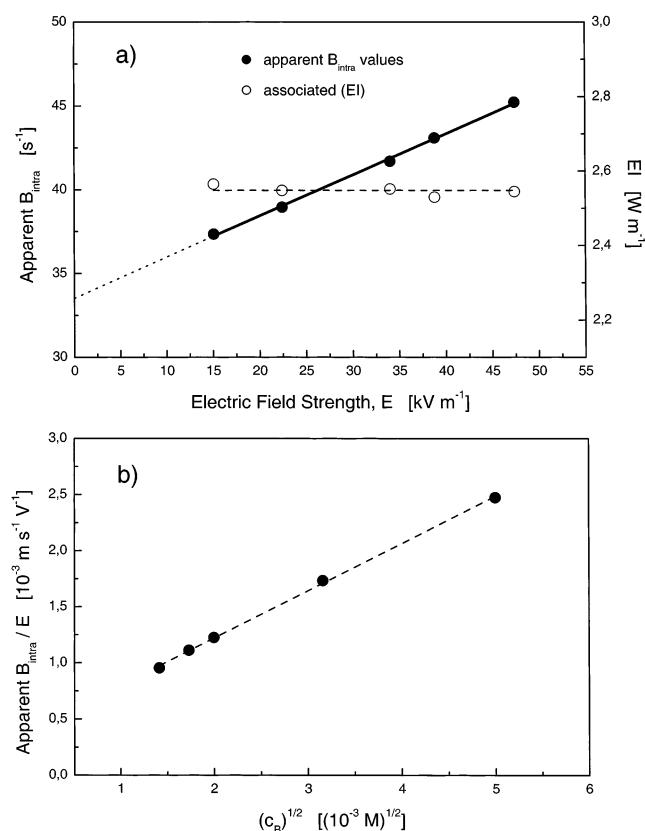


**Figure 9.** Intraparticle mass transfer kinetics with constant  $EI$  ( $2.54 \text{ W m}^{-1}$ ). Pressure gradient,  $\Delta P = 45 \text{ bar}$  ( $Pe = 145$ ). (a) While the electric field strength increases from  $15.1 \text{ kV m}^{-1}$  ( $c_B = 2.5 \times 10^{-2} \text{ M}$ ) to  $47.4 \text{ kV m}^{-1}$  ( $c_B = 2 \times 10^{-3} \text{ M}$ ), the electric current decreases from 169 to  $54 \mu\text{A}$  (cf. Table 2). (b)  $B_{\text{intra}}^{\text{app}}/E$  vs  $(c_B)^{1/2}$ .

**TABLE 2: Intraparticle Mass Transfer Characteristics ( $EI = \text{constant}$ )<sup>a</sup>**

$c_B [10^{-3} \text{ M}]$	2	3	4	10	25
$B_{\text{intra}}^{\text{app}} [\text{s}^{-1}]$ , eq 8	45.2	43.1	41.7	38.9	37.3
$\lambda_D [\text{nm}]$ , eq 1	3.9	3.2	2.7	1.7	1.1
$E [\text{kV m}^{-1}]$	47.4	38.8	34.1	22.5	15.1
$I [\mu\text{A}]$	54	65	75	113	169

<sup>a</sup> For all measurements  $EI = 2.54 \text{ W m}^{-1}$ ,  $Pe = 145$  ( $\Delta P = 45 \text{ bar}$ ), and  $Re = 0.36$ .

driven flow alone, but it is increased by the thermal effect ( $EI$ ). In fact,  $B_{\text{intra}}$  observed with only this pressure gradient comes close to that value ( $31.7 \text{ s}^{-1}$ , Figure 4c). Thus, probably due to the substantial pressure driven flow component ( $\Delta P = 45 \text{ bar}$ ,  $Pe = 150$ ) the additional electric field causes just a small increase in  $B_{\text{intra}}^{\text{app}}$  by a thermal effect. For example, the increase from  $B_{\text{intra}}^{\text{app}} = 37.3 \text{ s}^{-1}$  ( $2.5 \times 10^{-2} \text{ M}$ ) to  $45.2 \text{ s}^{-1}$  ( $2 \times 10^{-3} \text{ M}$ ) cannot be explained by diffusion, but must be due to convection (Figure 9a, Table 2). In Figure 9b the intraparticle mass transfer rate constant obtained for different  $c_B$  and  $E$  (but at a constant  $EI$ ) is normalized with respect to  $E$  and plotted against  $c_B$ . These data reveal a linear dependence of  $B_{\text{intra}}^{\text{app}}/E$  on  $(c_B)^{1/2}$  and they now clearly demonstrate experimentally (in view of eq 1) that double layer overlap (cf.  $\lambda_D$  in Tables 1 and 2) is relevant and important in our studies.<sup>84</sup> Still, the data cannot exclude that adsorption of monoborate ions on the particles surface may also play a role in this concentration range by increasing  $\zeta_p$  and the intraparticle EOF.

The results obtained so far indicate (i) negligible interparticle fluid resistance to mass transfer in EOF associated with the no-slip condition at the solid liquid interface (for  $r_{\text{pore}}/\lambda_D \gg$

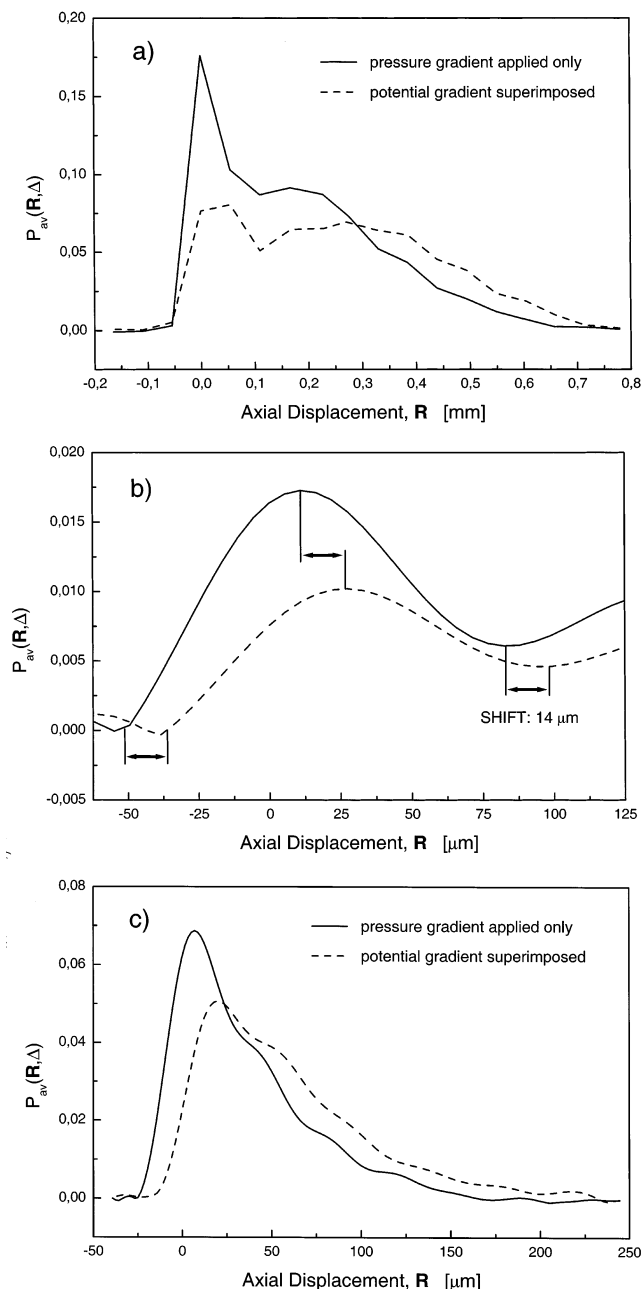


**Figure 10.** Effect on  $P_{\text{av}}(R, \Delta)$  of a superimposed potential gradient ( $E = 47.4 \text{ kV m}^{-1}$ ) in pressure driven flow,  $\Delta = 40 \text{ ms}$ . Pressure drop,  $\Delta P = 45 \text{ bar}$  ( $Pe = 145$ ): (a) Average propagator distribution obtained without zero-filling in  $q$ -space. (b) Focus on the region around zero displacement, raw data 10 times zero-filled. (c)  $\Delta P = 15 \text{ bar}$  ( $Pe = 50$ ). Mobile phase:  $2 \times 10^{-3} \text{ M}$  sodium tetraborate buffer.

1) and (ii) the existence of a significant intraparticle EOF. Unfortunately, the mass transfer kinetics does not directly reveal the actual velocity behind a convection-augmented  $B_{\text{intra}}^{\text{app}}$ . To determine the value of  $u_{\text{intra}}$  from our measurements, we focus on the resolved position of stagnant fluid in pressure driven flow depending on the superimposed potential gradient. In contrast to the purely diffusive mechanism, EOF is expected to provide a *net* shift in displacement as long as formerly stagnant fluid molecules can participate in the intraparticle flow over time  $\Delta$ .

Figure 10 compares displacement distributions obtained with only a pressure gradient and with an additional potential gradient. For example, Figure 10a clearly demonstrates that with the potential gradient the amount of fluid close to zero

displacement has decreased significantly and it also indicates that the distributions maximum here has shifted compared to the pressure driven flow (diffusive) reference. This is confirmed by Figure 10b which shows the region of interest after having zero-filled our raw data.<sup>87</sup> The peak that represents diffusion-limited fluid in hydraulic flow is indeed shifted (by ca. 14  $\mu\text{m}$ ) due to the additional electric field. It can only be explained by a convective electrokinetic driving force and means that, because most stagnant fluid is found *inside* the particles, the intraparticle EOF velocity seen in this shift is of the order of  $u_{\text{intra}} = 0.35$  mm/s ( $\Delta = 40$  ms). It is a substantial value keeping in mind that the average velocity in pure electrokinetic flow through the packed bed region “without” wall component is about  $u_{\text{eo}} = 0.69$  mm/s (Figure 5). Further, this latter value is probably an overestimate due to the much stronger thermal effect in pure electrokinetic flow ( $E = 47.4$  kV  $\text{m}^{-1}$ ;  $I = 53$   $\mu\text{A}$ ) and the wall effect. Thus, intraparticle and *true* interparticle EOF velocities are even closer.

As shown in Figure 10c a net shift is also visible at the lower Pe ( $\Delta P = 15$  bar) where intraparticle fluid is not as clearly resolved as with the higher Pe ( $\Delta P = 45$  bar). In both cases, however, the position of diffusion-limited fluid seen in the negative displacement tail of the propagator is very sensitive for a nonzero intraparticle EOF velocity. Given the fact that with the  $2 \times 10^{-3}$  M buffer solution we still encounter a considerable double layer overlap in the macroporous network of the particles,<sup>84</sup> the results shown in Figures 8–10 indicate an enormous potential for EOF in bulk transport of liquid through porous media. These data suggest that  $u_{\text{intra}}/u_{\text{inter}} \rightarrow 1$  under optimized conditions, leaving molecular diffusion as the ultimate limitation to performance. In pressure driven flow, by contrast, we usually have  $u_{\text{intra}}/u_{\text{inter}} \approx 0$ . That the displacement shift of intraparticle fluid indeed depends on the electrokinetic driving force is demonstrated by Figure 11. While the pressure gradient alone hardly achieves measurable intraparticle forced convection (Figure 11a), the increase of an additional potential gradient clearly shifts the ensemble of intraparticle fluid molecules to higher displacements (Figure 11b). This effect is rather systematic and an intraparticle Peclet number,  $\text{Pe}_{\text{intra}}$ , may be now estimated via the time constants for diffusion ( $\Delta_D = L^2/D_{\text{intra}}$ ) and convection ( $\Delta_C = L/u_{\text{intra}}$ ).<sup>88</sup> As characteristic dimension  $L$  we used  $r_p/3$ , i.e., the ratio of the spheres volume to its external surface<sup>63,82</sup>

$$\text{Pe}_{\text{intra}} = \frac{\Delta_D}{\Delta_C} = \frac{r_p u_{\text{intra}}}{3D_{\text{intra}}} \quad (10)$$

The data in Figures 8–11 demonstrate that due to the intraparticle EOF  $\text{Pe}_{\text{intra}}$  reaches values also above unity. Thus, convection becomes comparable to the diffusive mass flux already for the flow field molecules and will clearly dominate the intraparticle transport of solute molecules with a lower diffusivity. Diffusion-limited mass transfer practically vanishes when  $r_{\text{pore}}/\lambda_D \gg 1$ . It also implies that the effective particle diameter, usually defined with respect to diffusion-limited mass transfer, is drastically reduced below the physical  $d_p$  (41  $\mu\text{m}$ ) depending on the actual perfusive regime (e.g., on double layer overlap, pore size distribution, and pore interconnectivity) and has, thus, become a dynamic parameter.

After having been able to determine experimentally the intraparticle Peclet number  $\text{Pe}_{\text{intra}}$  in EOF through the packed capillary (Figures 10 and 11), complementary to the intraparticle mass transfer kinetics (Figures 8 and 9), one question is still unanswered: Is the increase in  $\text{Pe}_{\text{intra}}$  with  $c_B$  at constant  $EI$

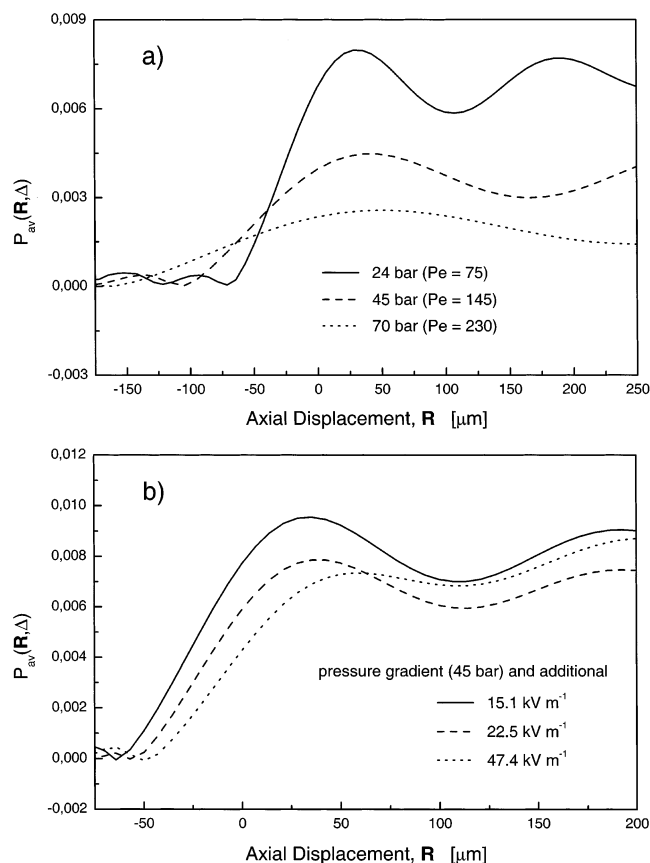


**Figure 11.** Net displacement of intraparticle fluid depending on the driving force. (a) Pressure gradient only with  $\Delta = 60$  ms. (b) Potential gradient superimposed on a constant pressure drop ( $\Delta = 50$  ms).

(Figure 9) only a consequence of suppressed double layer overlap (a mechanism that certainly contributes) or, in addition, does  $\zeta_p$  increase due to adsorption of borate ions on the particles surface? Borate ions are well-known to adsorb on certain (originally uncharged) organic polyols and other surfaces carrying hydroxy groups.<sup>89–93</sup>

This question has been answered by studying the particles surface electrokinetics ( $\zeta_p$ ) in dependence of  $c_B$ . For that purpose we have measured over a concentration range from  $3 \times 10^{-5}$  to  $4 \times 10^{-2}$  M sodium tetraborate streaming potentials ( $\Phi_{\text{str}}$ ) of porous plugs obtained with the packing material, using the system zeta potential analyzer SZP-06 from Müttek Analytic GmbH (Herrsching, Germany).  $\Phi_{\text{str}}$  can be obtained by forcing liquid flow inside the plug with an externally applied pressure gradient and measuring the generated potential difference.<sup>18</sup> Results are summarized in Table 3,  $\Gamma_B$  is the conductivity of the plug saturated with the respective buffer solution. Because liquid flow inside the particles is negligible compared to interparticle flow,  $\Phi_{\text{str}}$  characterizes the particles *external* surface. It has been shown that the mean size of interparticle voids ( $r_{\text{inter}}$ ) in sphere packings is about 25–40% of the particle size ( $r_p$ ).<sup>94,95</sup> Thus, in our case  $r_{\text{inter}} \approx 7$   $\mu\text{m}$  ( $d_p = 41$   $\mu\text{m}$ ) and, together with the Debye lengths (Table 3), we are in the limit of thin electric double layers over the whole concentration range ( $2 \times 10^2 < r_{\text{inter}}/\lambda_D < 8 \times 10^3$ ). Further, if surface conductivity of the particles is small compared to the bulk conductivity of the liquid, which is supported by a low surface-to-volume ratio of the interparticle pore space,  $\Phi_{\text{str}}$  can be related to  $\zeta_p$  by<sup>96</sup>

$$\left(\frac{\Phi_{\text{str}}}{\Delta P}\right)_{I=0} = \frac{\epsilon_0 \epsilon_r \zeta_p}{\Gamma_B \eta} \quad (11)$$

**TABLE 3: Plug Streaming Potentials and Mobile Phase Conductivities<sup>a</sup>**

$c_B$ [ $10^{-3}$ M]	0.03	0.1	0.2	0.5	1	2	5	10	20	40
$\Phi_{\text{str}}/\Delta P$ [ $10^{-7}$ V N $^{-1}$ m $^2$ ]	-4.1	-4.4	-4.35	-4.18	-3.49	-2.15	-1.09	-0.62	-0.26	-0.14
$\Gamma_B$ [ $10^{-4}$ S/cm]	0.06	0.15	0.36	0.83	1.58	3.05	6.71	11.8	25.6	43.1
$\lambda_D$ [nm], eq 1	31.9	17.5	12.4	7.8	5.5	3.9	2.5	1.7	1.2	0.9

<sup>a</sup> Values represent an average of two independent measurements at 25 °C.

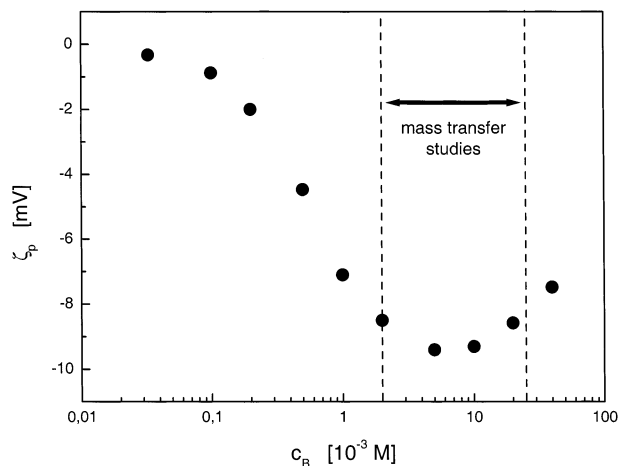


**Figure 12.** Electrokinetic characterization of the particles surface based on measurements of streaming potential factors ( $\Phi_{\text{str}}/\Delta P$ ) and conductivities (cf. Table 3) in plugs generated in situ.  $\zeta_p$  has been obtained with eq 11.

The result of this transformation is shown in Figure 12. The trend in these data clearly suggests that for  $10^{-4}$  M  $< c_B < 5 \times 10^{-3}$  M it is an adsorption of borate ions on the surface which substantially influences the electrokinetics. At low concentrations  $\zeta_p$  approaches a value close to zero, in agreement with the particles surface chemistry<sup>44,45</sup> indicating that a priori no significant charge should exist on this hydrophilic support when in contact with a liquid (unless the manufacturing process gives rise to charged impurities in/on the matrix). The aliphatic surface hydroxy groups are not dissociated at pH 9.13 and interparticle double layer overlap can be excluded as seen in Table 3. Due to promoted adsorption of borate ions  $\zeta_p$  increases with  $c_B$  (by a factor of almost 30!) until the adsorption capacity is approached. Then, above ca.  $10^{-2}$  M,  $\zeta_p$  begins to decrease with a further increasing  $c_B$  which represents the usual double layer behavior, i.e., addition of electrolyte compresses the double layer and therefore reduces  $\zeta_p$ .<sup>18</sup> It should be noted that values for  $\zeta_p$  in Figure 12 still include (via  $\Gamma_B$ ) the beds *electrokinetic* porosity and tortuosity. Thus, the actual  $\zeta_p$  is higher, the correction depending on contributions from inter- and intraparticle liquid.<sup>69,97</sup>

Complementary to this striking dependence of  $\zeta_p$  on  $c_B$ , PFG-NMR measurements of EOF through the packed capillary are shown in Figure 13 for three selected buffer concentrations. At  $c_B = 10^{-4}$  M, the fluid almost stands in the capillary ( $u_{\text{eo}} \approx 0.1$  mm/s only), while the EOF velocity increases by a factor of 3.5 at  $c_B = 5 \times 10^{-4}$  M and by a factor of 6 at  $c_B = 10^{-3}$  M compared to its value at  $10^{-4}$  M. Thus, relative velocities seen in the electroosmosis experiment (Figure 13) are in reasonable agreement with the dependence of  $\zeta_p$  on  $c_B$  resulting from the streaming potential measurements (Figure 12). It should be noted that, while surface conduction is often involved to explain anomalous electrokinetic behavior of, e.g., latex plugs,<sup>98–101</sup> we believe that borate adsorption also contributes to the trend in Figures 12 and 13, for the following reasons: (i) the interparticle surface-to-volume ratio is relatively low in our case compared to nanoparticles used in these electrokinetic studies,<sup>98,100,101</sup> (ii)

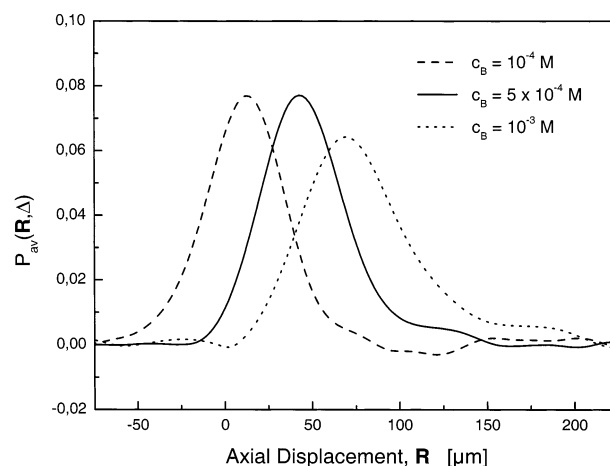


**Figure 13.** EOF through the packed capillary depending on the buffer concentration ( $\Delta = 120$  ms,  $E = 43.9$  kV m $^{-1}$ ). For  $c_B = 5 \times 10^{-4}$  M and  $c_B = 10^{-3}$  M the electrokinetic wall effect becomes visible again.

electroosmosis and streaming potential measurements give similar results, (iii)  $\zeta_p$  increases by a large factor of 30 in the range  $3 \times 10^{-5} \leq c_B \leq 5 \times 10^{-3}$  M, (iv) the particles surface should be originally uncharged which agrees well with  $\zeta_p \rightarrow 0$  at low  $c_B$ , and (v)  $\zeta_p$  values realized in our work ( $< 10$  mV, without a correction for the tortuosity and electrokinetic porosity, however) suggest that the surface charge density remains low. These arguments together indicate that conduction behind the shear plane, although possible and even probable,<sup>99</sup> is not necessarily the major or only contribution in the present case.

## Summary

PFG-NMR studies of electrokinetic flow phenomena in a packed capillary using a home-built configuration (Figure 2) first revealed an electrokinetic wall effect (Figures 5–7) in the attempt to measure, as in pressure driven flow (Figure 4), intraparticle mass transfer in pure electrokinetic flow. For the porous medium considered  $\zeta_w$  is much higher than  $\zeta_p$  and this causes a pronounced fronting in  $P_{\text{av}}(\mathbf{R}, \Delta)$  (Figure 7). Already these measurements indicated that intraparticle mass transfer is significantly faster than in pressure driven flow where we observed discrete bimodal propagator distributions representing stagnant and flowing fluid (Figure 4). In EOF, by contrast, we were unable to resolve intraparticle fluid and instead observed an exceptionally narrow (Figure 7c) Gaussian core in  $P_{\text{av}}(\mathbf{R}, \Delta)$  combined with the fronting wall component (Figures 5 and 7). Studies of  $B_{\text{intra}}^{\text{dp}}$  in electrokinetically driven flow were then achieved by superimposing a potential gradient on an already existing pressure gradient.  $B_{\text{intra}}^{\text{dp}}$  increased significantly under the influence of the potential gradient (Figure 8), most probably caused by a nonzero intraparticle EOF velocity. These data also raised the question of how far thermal effects (via the dependence of the molecular diffusion coefficient on temperature) could contribute to that increase. Clear proof of the existence and actual magnitude of an intraparticle Peclet number in EOF through the bed was provided by a series of measurements at a constant thermal level in the capillary, thus, with a



constant “diffusive background” (Figures 9–11). These data have shown that  $Pe_{\text{intra}} > 1$  in the present work and that  $u_{\text{intra}}/u_{\text{inter}} \rightarrow 1$  under optimized conditions. By contrast, we find  $u_{\text{intra}}/u_{\text{inter}} \rightarrow 0$  in pressure-driven flow (Figure 4a). Because  $\zeta_p$  was relatively low throughout this study  $Pe_{\text{intra}}$  did not exceed 10 and, therefore, fluid transport due to diffusion and convection remained comparable. The increase of  $B_{\text{intra}}^{\text{ap}}$  and  $Pe_{\text{intra}}$  with  $c_B$  can be explained by a suppression of double layer overlap (Tables 1 and 2) and adsorption of monoborate ions on the particles surface (Figures 12 and 13). However, the actual increase seen in Figures 9–11 is mainly due to reduced double layer overlap as  $\zeta_p$  is relatively independent of  $c_B$  in that range ( $2 \times 10^{-3} \leq c_B \leq 2.5 \times 10^{-2}$  M, cf. Figure 12). Our results not only clearly demonstrate advantages of EOF in bulk transport of liquid through porous media with a distribution of pore sizes (significant perfusion and negligible boundary layer mass transfer over a wide range of conditions) but have also indicated intrinsic problems such as thermal effects and the contribution of different surfaces (with their own electrokinetics) to volumetric flow and dispersion.

**Acknowledgment.** This research was supported by a Marie Curie Fellowship (for U.T.) under the Training and Mobility of Researchers Program TMR from the European Union (ERBFMBI-CT98-3437), by the European Community activity Large-Scale Facility Wageningen NMR Centre (ERBCHGE-CT95-0066), and by the Deutsche Forschungsgemeinschaft DFG (SE 586/7-1). U.T. likes to thank Prof. H. Poppe, Dr. W. Th. Kok and R. Stol (Department of Chemical Engineering, University of Amsterdam), and Ab J. van der Linde (Department of Physical and Colloid Chemistry, Wageningen University) for fruitful discussions. We are indebted to Dr. R. Nitzsche (Müttek Analytic GmbH, Herrsching, Germany) for the streaming potential measurements.

## References and Notes

- (1) Probstein, R. F. *Physicochemical Hydrodynamics: An Introduction*; John Wiley & Sons: New York, 1994.
- (2) Tsuda, T. *Electric Field Applications in Chromatography, Industrial and Chemical Processes*; VCH: Weinheim, 1995.
- (3) Rice, C. L.; Whitehead, R. J. *Phys. Chem.* **1965**, *69*, 4017.
- (4) Gross, R. J.; Osterle, J. F. *J. Chem. Phys.* **1968**, *49*, 228.
- (5) Griffiths, S. K.; Nilson, R. H. *Anal. Chem.* **1999**, *71*, 5522.
- (6) Liapis, A. I.; Grimes, B. A. *J. Colloid Interface Sci.* **2000**, *229*, 540.
- (7) Paul, P. H.; Garguilo, M. G.; Rakestraw, D. J. *Anal. Chem.* **1998**, *70*, 2459.
- (8) Tallarek, U.; Rapp, E.; Scheenen, T.; Bayer, E.; Van As, H. *Anal. Chem.* **2000**, *72*, 2292.
- (9) Dittmann, M. M.; Wienand, K.; Bek, F.; Rozing, G. P. *LC-GC* **1995**, *13*, 800.
- (10) Crego, A. L.; González, A.; Marina, M. L. *Crit. Rev. Anal. Chem.* **1996**, *26*, 261.
- (11) Colón, L. A.; Reynolds, K. J.; Alicea-Maldonado, R.; Fermier, A. M. *Electrophoresis* **1997**, *18*, 2162.
- (12) Fujimoto, C. *Trends Anal. Chem.* **1999**, *18*, 291.
- (13) Colón, L. A.; Burgos, G.; Maloney, T. D.; Citrón, J. M.; Rodríguez, R. L. *Electrophoresis* **2000**, *21*, 3965.
- (14) Shapiro, A. P.; Probstein, R. F. *Environ. Sci. Technol.* **1993**, *27*, 283.
- (15) Acar, Y. B.; Alshawabkeh, A. N. *Environ. Sci. Technol.* **1993**, *27*, 2638.
- (16) Acar, Y. B.; Gale, R. J.; Alshawabkeh, A. N.; Marks, R. E.; Puppala, S.; Bricka, M.; Parker, R. J. *Hazard. Mater.* **1995**, *40*, 117.
- (17) Ho, S. V.; Sheridan, P. W.; Athmer, C. J.; Heitkamp, M. A.; Brackin, J. M.; Weber, D.; Brodsky, P. H. *Environ. Sci. Technol.* **1995**, *29*, 2528.
- (18) Lyklema, J. *Fundamentals of Interface and Colloid Science, Vol. II: Solid-Liquid Interfaces*; Academic Press: London, 1995.
- (19) Sasidhar, V.; Ruckenstein, E. *J. Colloid Interface Sci.* **1982**, *85*, 332.
- (20) Hawkins-Cwirko, E.; Carbonell, R. G. *J. Colloid Interface Sci.* **1989**, *129*, 513.
- (21) Levine, S.; Neale, G. H. *J. Colloid Interface Sci.* **1974**, *47*, 520.
- (22) Kozak, M. W.; Davis, E. J. *J. Colloid Interface Sci.* **1986**, *112*, 403.
- (23) Ohshima, H. *J. Colloid Interface Sci.* **1999**, *210*, 397.
- (24) Jin, M.; Sharma, M. M. *J. Colloid Interface Sci.* **1991**, *142*, 61.
- (25) Coelho, D.; Shapiro, M.; Thovet, J. F.; Adler, P. M. *J. Colloid Interface Sci.* **1999**, *181*, 169.
- (26) Marino, S.; Coelho, D.; Békri, S.; Adler, P. M. *J. Colloid Interface Sci.* **2000**, *223*, 292.
- (27) Eykholt, G. R. *J. Hazard. Mater.* **1997**, *55*, 171.
- (28) Long, D.; Stone, H. A.; Ajdari, A. *J. Colloid Interface Sci.* **1999**, *212*, 338.
- (29) Herr, A. E.; Molho, J. I.; Santiago, J. G.; Mungal, M. G.; Kenny, T. W.; Garguilo, M. G. *Anal. Chem.* **2000**, *72*, 1053.
- (30) Rathore, A. S.; Horváth, Cs. *J. Chromatogr. A* **1997**, *781*, 185.
- (31) Liapis, A. I.; Grimes, B. A. *J. Chromatogr. A* **2000**, *877*, 181.
- (32) Li, D.; Remcho, V. T. *J. Microcolumn Sep.* **1997**, *9*, 389.
- (33) Venema, E.; Kraak, J. C.; Tijssen, R.; Poppe, H. *Chromatographia* **1998**, *58*, 347.
- (34) Venema, E.; Kraak, J. C.; Poppe, H.; Tijssen, R. *J. Chromatogr. A* **1999**, *837*, 3.
- (35) Stol, R.; Kok, W. Th.; Poppe, H. *J. Chromatogr. A* **1999**, *853*, 45.
- (36) Wen, E.; Asiaie, R.; Horváth, Cs. *J. Chromatogr. A* **1999**, *855*, 349.
- (37) Vallano, P. T.; Remcho, V. T. *Anal. Chem.* **2000**, *72*, 4255.
- (38) Tallarek, U.; Rapp, E.; Van As, H.; Bayer, E. *Angew. Chem. Int. Ed.* **2001**, *40*, 1684.
- (39) Stol, R.; Poppe, H.; Kok, W. Th. *Anal. Chem.* **2001**, *73*, 3332.
- (40) Stol, R.; Poppe, H.; Kok, W. Th. *J. Chromatogr. A* **2000**, *887*, 199.
- (41) Grimes, B. A.; Meyer, J. J.; Liapis, A. I. *J. Chromatogr. A* **2000**, *890*, 61.
- (42) Miller, N. P.; Berg, J. C.; O'Brien, R. W. *J. Colloid Interface Sci.* **1992**, *153*, 237.
- (43) Callaghan, P. T. *Principles of Nuclear Magnetic Resonance Microscopy*; Clarendon Press: Oxford, 1993.
- (44) Varady, L.; Mu, N.; Yang, Y.-B.; Cook, S. E.; Afeyan, N.; Regnier, F. E. *J. Chromatogr.* **1993**, *631*, 107.
- (45) Royappa, A. T. *J. Appl. Polym. Sci.* **1997**, *65*, 1897.
- (46) Frey, D. D.; Schweinheim, E.; Horváth, Cs. *Biotechnol. Prog.* **1993**, *9*, 273.
- (47) Afeyan, N. B.; Gordon, N. F.; Mazsaroff, I.; Varady, L.; Fulton, S. P.; Yang, Y. B.; Regnier, F. E. *J. Chromatogr.* **1990**, *519*, 1.
- (48) Rapp, E.; Bayer, E. *J. Chromatogr. A* **2000**, *887*, 367.
- (49) Pezron, E.; Leibler, L.; Ricard, A.; Lafuma, F.; Audebert, R. *Macromolecules* **1988**, *21*, 1121.
- (50) Ingri, N. *Acta Chem. Scand.* **1962**, *16*, 439.
- (51) Stejskal, E. O.; Tanner, J. E. *J. Chem. Phys.* **1965**, *42*, 288.
- (52) Kärger, J.; Heink, W. *J. Magn. Reson.* **1983**, *51*, 1.
- (53) Koch, D. L.; Brady, J. F. *J. Fluid Mech.* **1987**, *180*, 387.
- (54) Amin, M. H. G.; Gibbs, S. J.; Chorley, R. J.; Richards, K. S.; Carpenter, T. A.; Hall, L. D. *Proc. R. Soc. London A* **1997**, *453*, 489.
- (55) Seymour, J. D.; Callaghan, P. T. *AIChE J.* **1997**, *43*, 2096.
- (56) Sahimi, M. *Applications of Percolation Theory*; Taylor & Francis: London, 1994.
- (57) Tallarek, U.; van Dusschoten, D.; Van As, H.; Bayer, E.; Guiochon, G. *J. Phys. Chem. B* **1998**, *102*, 3486.
- (58) Tallarek, U.; Vergeldt, F. J.; Van As, H. *J. Phys. Chem. B* **1999**, *103*, 7654.
- (59) Neue, U. D. *HPLC Columns: Theory, Technology, and Practice*; Wiley-VCH: New York, 1997.
- (60) Bear, J. *Dynamics of Fluids in Porous Media*; Dover Publications: New York, 1988.
- (61) Kandhai, D.; Hlushkou, D.; Hoekstra, A. G.; Sloop, P. M. A.; Van As, H.; Tallarek, U. *Phys. Rev. Lett.* **2002**, *88*, article no. 234501.
- (62) Crank, J. *The Mathematics of Diffusion*; Clarendon Press: Oxford, 1956.
- (63) McCoy, M.; Kalghatgi, K.; Regnier, F. E.; Afeyan, N. *J. Chromatogr. A* **1996**, *743*, 221.
- (64) Nash, D. C.; Chase, H. A. *J. Chromatogr. A* **1998**, *807*, 185.
- (65) Whitney, D.; McCoy, M.; Gordon, N.; Afeyan, N. *J. Chromatogr. A* **1998**, *807*, 165.
- (66) Ruckenstein, E.; Vaidyanathan, A. S.; Youngquist, G. R. *Chem. Eng. Sci.* **1971**, *26*, 1305.
- (67) Carta, G.; Gregory, M. E.; Kirwan, D. J.; Massaldi, H. A. *Sep. Technol.* **1992**, *2*, 62.
- (68) Choudhary, G.; Horváth, Cs. *J. Chromatogr. A* **1997**, *781*, 161.
- (69) Rathore, A. S.; Wen, E.; Horváth, Cs. *Anal. Chem.* **1999**, *71*, 2633.
- (70) Liu, Y.; Pietrzyk, D. J. *Anal. Chem.* **2000**, *72*, 5930.
- (71) Rathore, A. S.; Horváth, Cs. *Anal. Chem.* **1998**, *70*, 3069.
- (72) Neale, G.; Epstein, N.; Nader, W. *Chem. Eng. Sci.* **1973**, *28*, 1865.

- (73) Bey, O.; Eigenberger, G. *Chem. Eng. Sci.* **1997**, *52*, 1365.
- (74) Giese, M.; Rottschäfer, K.; Vortmeyer, D. *AIChE J.* **1998**, *44*, 484.
- (75) Tallarek, U.; Scheenen, T. W. J.; Van As, H. *J. Phys. Chem. B* **2001**, *105*, 8591.
- (76) Locke, B. R.; Acton, M.; Gibbs, S. J. *Langmuir* **2001**, *17*, 6771.
- (77) Sederman, A. J.; Alexander, P.; Gladden, L. F. *Powder Technol.* **2001**, *117*, 255.
- (78) Stephanopoulos, G.; Tsiveriotis, K. *Chem. Eng. Sci.* **1989**, *44*, 2031.
- (79) Lu, Z. P.; Dias, M. M.; Lopes, J. C. B.; Carta, G.; Rodrigues, A. E. *Ind. Eng. Chem. Res.* **1993**, *32*, 1839.
- (80) Xu, Y.; Liapis, A. I. *J. Chromatogr. A* **1996**, *724*, 13.
- (81) Rodrigues, A. E.; Ahn, B. J.; Zoulalian, A. *AIChE J.* **1982**, *28*, 541.
- (82) Rodrigues, A. E.; Lopes, J. C.; Lu, Z. P.; Loureiro, J. M.; Dias, M. M. *J. Chromatogr.* **1992**, *590*, 93.
- (83) Leitão, A.; Rodrigues, A. *Chem. Eng. J.* **1995**, *60*, 81.
- (84) Wan, Q.-H. *Anal. Chem.* **1997**, *69*, 361.
- (85) Happel, J.; Brenner, H. *Low Reynolds Number Hydrodynamics*; Martinus Nijhoff: The Hague, 1983.
- (86) Boyd, G. E.; Adamson, A. W.; Meyers, L. S., Jr. *J. Am. Chem. Soc.* **1947**, *69*, 2836.
- (87) Marshall, A. G.; Verdun, F. R. *Fourier Transforms in NMR, Optical, and Mass Spectrometry*; Elsevier: Amsterdam, 1990.
- (88) Nir, A.; Pismen, L. M. *Chem. Eng. Sci.* **1977**, *32*, 35.
- (89) Barrow, N. J. *J. Soil Sci.* **1989**, *40*, 427.
- (90) Keren, R.; Grossl, P. R.; Sparks, D. L. *Soil Sci. Soc. Am. J.* **1994**, *58*, 1116.
- (91) Sinton, S. W. *Macromolecules* **1987**, *20*, 2430.
- (92) Smith, B. M.; Todd, P.; Bowman, C. N. *Sep. Sci. Technol.* **1999**, *34*, 1925.
- (93) Lin, H.-L.; Yu, T. L.; Cheng, C.-H. *Colloid Polym. Sci.* **2000**, *278*, 187.
- (94) Knox, J. H.; Scott, H. P. *J. Chromatogr.* **1984**, *316*, 311.
- (95) Dullien, F. A. L. *Porous Media: Fluid Transport and Pore Structure*; Academic Press: San Diego, 1992.
- (96) Overbeek, J. Th. G. Electrokinetic Phenomena. In *Colloid Science*; Kruyt, H. R., Ed.; Elsevier: Amsterdam, 1952.
- (97) Vallano, P. T.; Remcho, V. T. *J. Phys. Chem. B* **2001**, *105*, 3223.
- (98) Van der Put, A. G.; Bijsterbosch, B. H. *J. Colloid Interface Sci.* **1983**, *92*, 499.
- (99) Lyklema, J.; Minor, M. *Colloids Surf. A* **1998**, *140*, 33.
- (100) Folkersma, R.; van Diemen, A. J. G.; Stein, H. N. *Langmuir* **1998**, *14*, 5973.
- (101) Löbbus, M.; van Leeuwen, H. P.; Lyklema, J. *Colloids Surf. A* **2000**, *161*, 103.